

Estimating the warm dark matter mass from strong lensing images with truncated marginal neural ratio estimation

Noemi Anau Montel¹★, Adam Coogan^{1,2,3}†, Camila Correa¹, Konstantin Karchev^{1,4}, Christoph Weniger¹‡

¹GRAPPA (Gravitation Astroparticle Physics Amsterdam), University of Amsterdam, Science Park 904, 1098 XH Amsterdam, The Netherlands

²Département de Physique, Université de Montréal, 1375 Avenue Thérèse-Lavoie-Roux, Montréal, QC H2V 0B3, Canada

³Mila – Quebec AI Institute, 6666 St-Urbain, 200, Montreal, QC, H2S 3H1

⁴SISSA (Scuola Internazionale Superiore di Studi Avanzati), via Bonomea 265, I-34136 Trieste, Italy.

Accepted XXX. Received YYY; in original form ZZZ

ABSTRACT

Precision analysis of galaxy-galaxy strong gravitational lensing images provides a unique way of characterizing small-scale dark matter halos, and could allow us to uncover the fundamental properties of dark matter’s constituents. In recent years, gravitational imaging techniques made it possible to detect a few heavy subhalos. However, gravitational lenses contain numerous subhalos and line-of-sight halos, whose subtle imprint is extremely difficult to detect individually. Existing methods for marginalizing over this large population of sub-threshold perturbers in order to infer population-level parameters are typically computationally expensive, or require compressing observations into hand-crafted summary statistics, such as a power spectrum of residuals. In this work we present the first analysis pipeline to combine parametric lensing models and a recently-developed neural simulation-based inference technique called truncated marginal neural ratio estimation (TMNRE) to constrain the warm dark matter halo mass function cutoff scale directly from multiple lensing images. Through a proof-of-concept application to simulated data, we show that our approach enables empirically testable inference of the dark matter cutoff mass through marginalization over a large population of realistic perturbers that would be undetectable on their own, and over lens and source parameters uncertainties. To obtain our results, we combine the signal contained in a set of images with Hubble Space Telescope resolution. Our results suggest that TMNRE can be a powerful approach to put tight constraints on the mass of warm dark matter in the multi-keV regime, which will be relevant both for existing lensing data and in the large sample of lenses that will be delivered by near-future telescopes.

Key words: dark matter – gravitational lensing: strong – methods: statistical

1 INTRODUCTION

Over the past several decades, numerous astrophysical probes including rotational curves of spiral galaxies (Rubin et al. 1980), galaxy-cluster dynamics (Zwicky 1933), cosmic microwave background (Ade et al. 2016), gravitational lensing observations (Taylor et al. 1998), have established dark matter (DM) as one of the major components of the Universe. However, up to the present time, the fundamental nature of DM is still an unresolved puzzle. For many years, the cold dark matter (CDM) paradigm (Peebles 1982) has been able to accurately reproduce vastly disparate large scale observations across all epochs. In this model, DM is massive, neutral, non-relativistic, and collisionless. The main prediction of the CDM paradigm is that structure formation is due to a hierarchical clustering process, guided by gravitational instability of DM density perturbations, originated from quantum fluctuations during inflation.

Despite providing a stunning description of the observed distribu-

tion of matter on large scales ($> O(\text{Mpc})$), the agreement between CDM predictions and observations at galactic and sub-galactic scales has been less clear. One of the most well-known small-scales discrepancies of CDM is the missing satellites problem (Moore et al. 1999). Numerical CDM simulations predict that a large population of DM subhalos, spanning a wide range of masses, should be orbiting around all main DM halos. However, we have observed a lot fewer small galaxies in the Local Group than the predicted subhalos below $10^9 M_\odot$ (Klypin et al. 1999).

Solutions to this tension include the impact of baryonic processes or alternative DM physics. Baryonic processes from supernovae feedback and reionization processes suppress star formation in low-mass galaxies (Bullock 2010). As a result, most DM subhalos would not contain sufficiently bright galaxies and thus are more difficult to detect. The other approach requires an alteration of DM particle physics, such that large-scale predictions remain unaffected, but the number of small-scale substructures is suppressed. One of the alternative models that has been proposed is warm dark matter (WDM) (Colin et al. 2000; Lovell et al. 2014). Moreover, its main particle candidates, sterile neutrinos (Boyarsky et al. 2019) and gravitinos (Bond et al. 1982), are well-motivated from a particle physics perspective. In

★ Email: n.anaumontel@uva.nl

† Email: adam.coogan@umontreal.ca

‡ Email: c.weniger@uva.nl

WDM models DM particles have non-negligible thermal velocities that allow them to free-stream out of density perturbations, effectively preventing small-scale structure formation. The scale at which this happens depends on model parameters and is parametrised by the half-mode mass M_{hm} in the halo mass function (HMF). Therefore, one of the viable way to discriminate between CDM and alternative DM models is to constrain the low-mass end of the HMF by probing small-scale DM halos which are completely devoid of stars and truly *dark*, whose only signature is then gravitational.

Strong lensing images analysis. In strong gravitational lensing, the gravitational field of a mass distribution acts as a lens by distorting and magnifying the light flux coming from a foreground source (Kochanek 2004). This effect is sensitive only to how matter is distributed, regardless of its physical nature (baryonic/DM). Hence, it provides a direct way of probing the distribution of DM at small scales, by means of the distortions to the images due to substructures on top of the main lens mass distribution. Therefore, gravitational lensing provides a pristine probe of small-scale structures and can in principle distinguish between CDM and WDM scenarios.

Various different methods have been suggested to analyse the effects of small-scale structures on lensing images (Drlica-Wagner et al. 2019). These methods usually target two different types of lensing systems that differ in the lensed source: extended background galaxies that get lensed into extended arcs or complete Einstein rings, and almost point-like quasars that get lensed into multiple point-like projections.

Quasar lensing was first used in Mao & Schneider (1998) to constrain the amount of DM substructures by analysing the deviations in the relative fluxes of the multiple source projections from a smooth lens model. Later, Dalal & Kochanek (2002) derived a statistical constraint on the substructure fraction in the lensing galaxies using a small sample of seven lensed quasars. Nierenberg et al. (2014) showed that flux-ratio anomalies can also be used to detect individual low-mass subhalos. Several studies derived upper limits on the half-mode mass M_{hm} (Nierenberg et al. 2017; Gilman et al. 2018), also including perturbations due to line-of-sight (LOS) halos (Gilman et al. 2019a,b). Further investigations (Hsueh et al. 2016, 2017, 2019) pointed out the importance of correctly modelling baryonic structure in the main lens, in order to avoid systematic errors while constraining DM substructure abundance with flux-ratio anomalies.

On the other hand, in strong-lens systems where the background source is a galaxy, massive substructures can leave a signature in the form of percent-level variations in the shape of the predicted lensed light based on a smooth lens model. The gravitational imaging technique, which models these distortions, was first introduced in Koopmans (2005) and further developed in Vegetti & Koopmans (2009a,b). Its application to real data has lead to several detections of individual heavy ($> 10^8 M_{\odot}$) subhalos (Vegetti et al. 2010a,b, 2012; Hezaveh et al. 2016a). Moreover, samples of gravitational lens systems have been analyzed in Vegetti et al. (2014, 2018), and, including LOS halos modelling, in Ritondale et al. (2019), in order to derive constraints on the HMF using detections and non-detections of individual substructures.

A population of low-mass halos can collectively cause perturbations to images that can be detected statistically in order to constrain the HMF. In reality, constraining collective substructure properties from gravitational lensing images is an extremely difficult problem. In fact, inferring marginal posteriors for the HMF cutoff requires marginalizing over all source, lens, and substructures parameters to get the marginal likelihood for the population-level parameter of interest, thus involving a time-consuming exploration of a very high-

dimensional parameter space for complex realistic models. Therefore, Markov chain Monte-Carlo (MCMC) or nested sampling methods would imply an intractable sampling from the high-dimensional joint posterior.

To partially overcome traditional likelihood-based methods' challenges, Brewer et al. (2015) and Daylan et al. (2018) performed inference on subhalos using a likelihood-based method called transdimensional Bayesian inference. This approach uses transdimensional MCMC sampling over the union of different models, with different numbers of subhalos, to infer a probability for the subhalos catalog.

In order to reduce the dimensionality of the problem and enable inference of the collective effects of a large number of low-mass substructures at the statistical level, Hezaveh et al. (2016b) proposed to use the power spectrum (PS) of the lensed deflection field. Subsequently, Diaz Rivero et al. (2018) developed a theoretical general formalism to compute the convergence PS for different subhalo populations from first principles, which was adopted in Diaz Rivero et al. (2018) and Brennan et al. (2019). This formalism has been recently expanded to account for LOS halos in Çağan Şengül et al. (2020). However, this approach is not directly applicable to observations, because we do not have access to the true displacement field from the data. Chatterjee & Koopmans (2017), Bayer et al. (2018) and Cyr-Racine et al. (2019) developed statistical formalisms to relate PS of the surface brightness fluctuations in strong lens images to the lens potential fluctuations arising from DM distribution, that contribute to the convergence PS. And Bayer et al. (2018) applied it to a real observation.

Instead, Birrer et al. (2017) and He et al. (2020) employed the residual PS summary statistic, given by the subtraction of a smooth lens model from the data, to constrain the half-mode mass M_{hm} . For the analysis they used approximate Bayesian computation (ABC), a likelihood-free inference method based on a rejection algorithm (Grazian & Fan 2019).

Another class of methods that has developed in recent years uses neural networks to measure lens parameters (Hezaveh et al. 2017; Perreault Levasseur et al. 2017; Morningstar et al. 2019), detect individual subhalos (Diaz Rivero & Dvorkin 2020), and distinguish different types of DM substructure (Alexander et al. 2020). Still, these methods need lots of data to amortize over all possible variations in lensing systems. In fact, amortized methods learn the posterior for any data, generated by any parameter. But learning an amortized posterior is unnecessary if only a small range of parameters are consistent with a target observation.

In this work we present the first analysis pipeline that combines parametric lensing models with recent neural simulation based inference (SBI) developments (Cranmer et al. 2020) to infer the DM mass cutoff scale from a set of realistic simulated galaxy-galaxy strong lenses, by combining their signal. In fact, there are currently around a hundred strong lensing observations suitable for substructure inference, most of which come from the SLACS (Bolton et al. 2006) and BELLS (Brownstein et al. 2011) surveys. In the near future, new and future telescopes like JWST (Gardner et al. 2006), ELT (Simon et al. 2019), Euclid (Refregier et al. 2010; Laureijs et al. 2011), SKA (Koopmans et al. 2004), and LSST (Abolfathi et al. 2021) will deliver thousands of very high precision galaxy-galaxy lensing images (McKean et al. 2015). It is then extremely important to be able to combine the information coming from different observations in the statistical analysis.

For the statistical analysis we employ truncated marginal neural ratio estimation (TMNRE). Developed by Hermans et al. (2020) and Miller et al. (2020), marginal neural ratio estimation (MNRE) is a

neural SBI method that makes it possible to learn the marginal posterior approximation for a specified subset of model parameters of interest directly from the full input data that, in our case, corresponds to the observed lensed images, without the need for hand-crafted summary statistics. This method improves the simulator efficiency and the quality of inference. Moreover, MNRE is amortized, which enables important statistical tests. Up to now, this approach has been applied in simplified modelling frameworks: [Hermans et al. \(2020\)](#) focuses on recovering the Einstein radius of a gravitational lens marginalizing over 15 source and lens mass distribution parameters, whereas [Brehmer et al. \(2019\)](#) estimates the slope and normalization of a CDM subhalo mass function. SBI using neural posterior density estimator and hierarchical inference have also been employed in [Wagner-Carena et al. \(2022\)](#) to infer the CDM subhalo mass function normalization from a set of strong-lensing images, generated using real galaxy images as a source model, including realistic observational noise effects from Hubble Space Telescope (HST) and accounting for the mean expected convergence from LOS halos.

TMNRE is able to *target* the inference to a specific observation at hand rather than amortize over all possible parameters combinations, by successively focusing simulations on the parameter regions that are most relevant for the inference problem ([Miller et al. 2021](#)). This targeted approach is more efficient when most posterior density is concentrated compared to the prior density, which is the case for lens and source parameters. This truncation method applied to strong-lensing images was proposed in [Karchev et al. \(2021\)](#) and used in [Coogan et al. \(2020, 2022\)](#) to learn marginal posterior approximations for individual subhalo parameters, marginalizing over lens and source uncertainties given an observation. It has also been recently applied to analysis of the CMB ([Cole et al. 2021](#)).

The main goal of this work is to demonstrate that our TMNRE approach is sensitive to the HMF half-mode mass M_{hm} given a set of HST resolution observations, and it is able to efficiently and accurately infer its statistic.

The paper is structured as follows. In [section 2](#) we describe how we model strong-lens observations with analytic source, lens and substructure population that accounts for both subhalos and LOS halos. In [section 3](#) we discuss the inference methodology employed in the statistical analysis: TMNRE. Finally, we show our results in [section 4](#) and conclude in [section 5](#). This work paves the way for combining the presented statistical analysis with more realistic strong lensing source models and for future applications to real high-resolution data in upcoming works.

2 STRONG-LENSING MODEL

In this section, we review how we model strong lensing images. In strong-lensing systems the mass distribution of a foreground galaxy gravitationally lenses the light rays coming from a background source, resulting in an arc-like image in the case of an extended galaxy source. Under the assumptions of the thin-lens formalism ([Meneghetti 2016](#)), the lens-plane and source-plane coordinates of a light ray, respectively $\vec{\xi}$ and \vec{x} , are related by the simple raytracing equation:

$$\vec{x} = \vec{\xi} - \vec{\alpha}(\vec{\xi}). \quad (1)$$

The displacement field $\vec{\alpha}$ can be computed as

$$\vec{\alpha}(\vec{\xi}) = \frac{4G}{c^2} \frac{D_{ls}}{D_l D_s} \int d^2(D_l \vec{\xi}') \frac{\vec{\xi} - \vec{\xi}'}{|\vec{\xi} - \vec{\xi}'|^2} \Sigma(\vec{\xi}'), \quad (2)$$

where we have introduced the angular diameter distance from the observer to the lens D_l , from the observer to the source D_s , and from the lens to the source D_{ls} . The projected mass density is given by the integral of the 3D lensing mass density ρ :

$$\Sigma(\vec{\xi}) = \int dz \rho(\vec{\xi}, z), \quad (3)$$

where z is the coordinate perpendicular to the lens plane. It is also useful to define the convergence κ in terms of the critical surface density $\Sigma_{\text{cr},l}$ on the lens plane as:

$$\kappa(\vec{\xi}) = \frac{\Sigma(\vec{\xi})}{\Sigma_{\text{cr},l}}, \quad \Sigma_{\text{cr},l} \equiv \frac{c^2}{4\pi G} \frac{D_s}{D_l D_{ls}}, \quad (4)$$

where c is the speed of light and G is the gravitational constant. It can be shown that the convergence κ is related to the trace of the Jacobian of the lensing transformation, and it represents the lens mass distribution.

Strong-lensing systems are then represented by two main ingredients: the lens model, which describes the total mass distribution of the lens, and the source model, which describes the surface brightness profile of the background source. It is common to split the lens model into a macroscopic smooth component (main lens and external shear) and a substructure¹ component, due to subhalos and LOS halos. Each ingredient can be directly superimposed by summing their respective displacement fields in the lens plane:

$$\vec{\alpha} = \vec{\alpha}_{\text{lens}} + \vec{\alpha}_{\text{ext}} + \sum_{i=1}^{N_{\text{sub}}} \vec{\alpha}_{\text{sub},i} + \sum_{i=1}^{N_{\text{los}}} \vec{\alpha}_{\text{los},i}. \quad (5)$$

In the following subsections we will describe each component of the model, which we summarize in [Table 1](#).

2.1 Main lens model

We model the lens mass distribution smooth component with a singular power-law ellipsoid (SPLE) lens ([Suyu et al. 2009](#)) plus external shear. The latter account for matter in the lens surroundings and describes large-scale effects constant across the image. For a detailed description of these two ingredients we refer the reader to [Karchev et al. \(2021\)](#). We end up with eight parameters in total that we collect in the vector $\theta_l \equiv \{r_{\text{Ein}}, \xi_{0,x}, \xi_{0,y}, q_l, \phi_l, \gamma, \gamma_1, \gamma_2\}$, the first six from the SPLE for the main-lens mass distribution and the last two for external shear.

When simulating data (see [subsection 4.1](#)), we always use the same SPLE slope that produced the mock observation we are analysing (as fixed in [Table 1](#)) instead of inferring it.²

2.2 Source model

To model the surface brightness of the source galaxy, we adopt a Sérsic profile ([Sérsic 1963](#)). The surface brightness distribution is

¹ Throughout our work, we use the terms ‘small-scale structures’, ‘substructures’, and ‘low-mass halos’ when considering both subhalos of the main lens and LOS halos.

² The reason why we fix the SPLE slope is that it has a complex degeneracy with the source in part due to the mass-sheet transformation ([Schneider & Sluse 2014; Unruh et al. 2017](#)), which requires additional information about lensing and stellar kinematics properties in order to be broken ([Barnabe & Koopmans 2007; Enzi et al. 2020](#)).

Table 1. Summary of model parameters used for the simulated images in this work. When a prior distribution is not specified, the parameter is fixed to the true value.

Parameter	True value	Prior	Description
Main lens			
r_{Ein} ["]		$\mathcal{U}(1., 2.)$	SPLE Einstein radius
$\xi_{0,x}$ ["]		$\mathcal{U}(-0.2, 0.2)$	lens center x axis
$\xi_{0,y}$ ["]		$\mathcal{U}(-0.2, 0.2)$	lens center y axis
q_l		$\mathcal{U}(0.1, 1.)$	axis ratio
ϕ_l [rad]		$\mathcal{U}(0, 2\pi)$	rotation angle
γ	2.1	-	slope
z_{lens}	0.5	-	lens redshift
External shear			
γ_1		$\mathcal{U}(-0.05, 0.05)$	1 st component
γ_2		$\mathcal{U}(-0.05, 0.05)$	2 nd component
Source			
I_e		$\mathcal{U}(0., 4.)$	Sérsic surface intensity
r_e ["]		$\mathcal{U}(0.1, 2.5)$	effective radius
x_0 ["]		$\mathcal{U}(-0.1, 0.1)$	source center x axis
y_0 ["]		$\mathcal{U}(-0.1, 0.1)$	source center y axis
q_s		$\mathcal{U}(0.1, 1.)$	axis ratio
ϕ_s [rad]		$\mathcal{U}(0, 2\pi)$	position angle
n		$\mathcal{U}(0.1, 4.)$	index
z_{src}	2	-	source redshift
Subhalos			
\vec{p} ["]	$\in [-2.5, 2.5]$	$\mathcal{U}_{2D}(-2.5, 2.5)$	tNFW position
m_{200} [M_\odot]	$\in [10^7, 10^{10}]$	Giocoli et al. (2010)	virial mass
c_{200}	15.	-	concentration
τ	6.	-	truncation
LOS halos			
\vec{p} ["]	$\in [-2.5, 2.5]$	$\mathcal{U}_{2D}(-2.5, 2.5)$	projected tNFW position
m_{200} [M_\odot]	$\in [10^7, 10^{10}]$	Tinker et al. (2008)	virial mass
z_{LOS}	$\in [0, z_{\text{src}}]$	Tinker et al. (2008)	LOS redshift
c_{200}	15.	-	concentration
τ	6.	-	truncation
WDM			
M_{hm} [M_\odot]		$\log \mathcal{U}(10^7, 10^{10})$	half-mode mass

given by

$$\beta(x, y) = I_e \exp \left\{ -k_n \left[\left(\frac{r(x, y)}{r_e} \right)^{1/n} - 1 \right] \right\}, \quad (6)$$

where I_e is the surface intensity at the half-light radius r_e , $r(x, y) = \sqrt{r_x^2 + r_y^2}$ is the elliptical radial coordinate, and the normalization k_n depends on the index n . We give more details about the Sérsic profile modelling and parameters in appendix A. In total, the analytic source is parameterized with seven variables that we collect in the vector $\theta_s \equiv \{I_e, r_e, x_0, y_0, q_s, \phi_s, n\}$.

2.3 Small-scale structures model

Substructures can be divided into two categories: subhalos that orbit around the main halo at the lens redshift, and LOS halos distributed between the source and the observer. LOS halos are a more direct probe of free-streaming-induced small-scale structure suppression, because they are not affected by tidal effects and the presence of baryons. For this reason and the fact that they are expected to be more abundant than subhalos in a lensing system (Despali et al. 2018; He et al. 2021), it is very important to model them as well, in order to correctly estimate the collective effects of all substructures on the lensing image.

2.3.1 Density profile

To model the density profiles of small-scale DM halos we adopt the smoothly truncated universal 3D mass density profile from Baltz et al. (2009):

$$\rho_{\text{tNFW}}(r) = \frac{\rho_s}{r/r_s(1+r/r_s)^2} \frac{1}{1+(r/r_t)^2}. \quad (7)$$

Here r is the three-dimensional distance from the center of the halo, ρ_s and r_s are respectively the scale density and scale radius that specify an Navarro-Frenk-White (NFW) profile (Navarro et al. 1997), and $r_t \equiv \tau r_s$ is the tidal truncation radius that depends on the history of the subhalo. Typical values of the truncation scale τ range from 4 – 10 for spherically symmetric lenses (Gilman et al. 2019b; Cyr-Racine et al. 2019); we fix $\tau = 6$ for simplicity. Compared to the standard NFW form, which has an infinite total mass, the truncated NFW (tNFW) contains an additional truncation term which makes the profile decay as r^{-5} for large radii, resulting in a finite total mass given by:

$$m_\tau = 4\pi\rho_s r_s^3 \frac{\tau^2}{(\tau^2 + 1)^2} [(\tau^2 - 1) \ln \tau + \tau\pi - (\tau^2 + 1)]. \quad (8)$$

With a fixed truncation scale, the tNFW profile is fully determined by the same parameters that determine the NFW profile: the virial mass m_{200} ³ and the concentration $c_{200} = r_{200}/r_s$ of the halo. The latter measures how concentrated the mass of a halo is and fixes the density normalization; in principle it varies from one subhalo to the next and shows dependencies on mass and redshift of the main halo. In this paper, instead of adopting a concentration-mass relation, we fix $c_{200} = 15$ in accordance with Richings et al. (2021). We would like to note that accounting for the scatter in the mass-concentration relation might boost the expected lensing signal from a low-mass halo (Amorisco et al. 2021).

LOS halos are also modelled with a tNFW profile following the prescription by Çağan Şengül et al. (2020), that shows how to treat halos along the line-of-sight as effective subhalos on the main-lens plane, with a modified scale radius and mass. We give more details on this procedure in appendix B. For LOS halos we adopt the same concentration and truncation scale values used for subhalos.

The equations for calculating the displacement field of a tNFW halo, given its mass and position, are fully elaborated by Baltz et al. (2009, Appendix A).

2.3.2 Mass and spatial distributions

We sample subhalo masses from the CDM mass function of Giocoli et al. (2010):

$$\frac{1}{M} \frac{dn_{\text{sub}}(m_{200}, z)}{d \log m_{200}} \propto (1+z)^{1/2} m_{200}^\alpha \exp \left[-\beta \left(\frac{m_{200}}{M} \right)^3 \right], \quad (9)$$

where M is the main halo's mass and m_{200} the subhalo mass. We use the normalization, slope and exponential cutoff of the subhalo mass function from Despali & Vegetti (2017). For LOS halos masses we use the Tinker et al. (2008) CDM halo mass function assuming an overdensity with respect to the critical density of the Universe at the epoch of analysis of $\Delta = 200$. For both subhalos and LOS halos we adopt the following mass range, with $m_{200, \text{min}} = 10^7 M_\odot$

³ We parameterize subhalos by what would be their mass up to the virial radius r_{200} using the untruncated profile, with the same central density ρ_s and scale radius r_s as the truncated one.

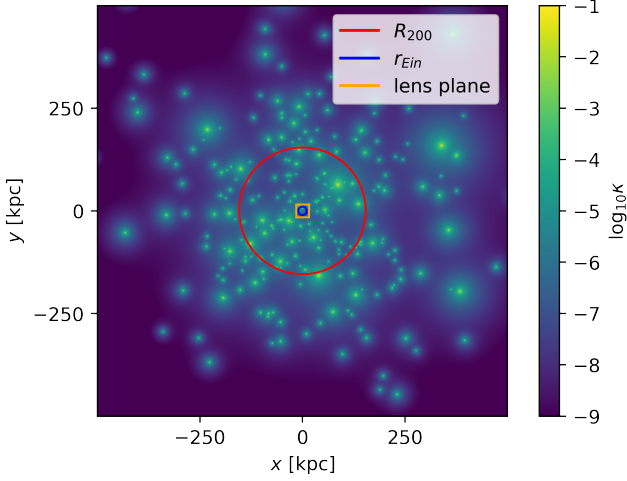


Figure 1. Convergence map for a CDM subhalo population in the adopted mass range. The convergence map shows how the deflecting mass from all the subhalo lenses is distributed. The full map size is 1×1 Mpc. We mark in red the virial radius of the main lens halo, in blue its Einstein radius, and in orange the 5×5 arcsec lens plane.

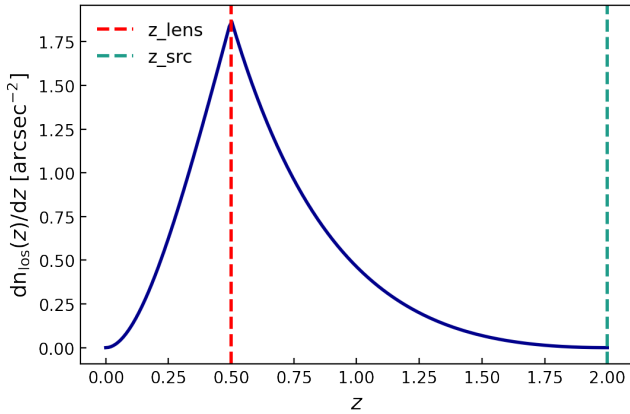


Figure 2. LOS halos distribution in redshift for our source and lens redshifts configuration, described in Table 1.

and $m_{200,\max} = 10^{10} M_{\odot}$. The upper limit is chosen based on the assumption that more massive halos would be visible and could therefore be modelled independently. The lower one is fiducial, and we plan on investigating more the sensitivity of our inference in the future.

The spatial distribution of subhalos has been shown to follow an Einasto profile (Springel et al. 2008). However, since the virial radius of a typical main lens halo is much larger than its Einstein radius, and hence, than the image plane, we approximate the distribution to be uniform in the lens plane. Still, we derive the total number of expected subhalos within the image via the Einasto fit of Despali & Vegetti (2017). We find that on average 4 subhalos fall within the lens plane in our adopted lensing configuration and mass range. In Figure 1 we show the convergence map for one realization of our subhalo population.

LOS halos are rendered in a double-cone geometry with the lens plane as an opening angle, and closing angle such that the cone

closes at the source redshift, as described in Çağan Şengül et al. (2020, Figure 3). We infer the number of detectable LOS halos by integrating their mass function in the mass range adopted for the analysis and within the double-cone volume

$$N_{\text{los}} = \int_0^{z_{\text{src}}} \int_{m_{200,\min}}^{m_{200,\max}} n_{\text{los}}(m_{200}, z) dm_{200} \frac{dV}{dz}. \quad (10)$$

On average we get 260 LOS halos projected in our lens plane. In Figure 2 we show the distribution of LOS in redshift for our lens and source redshifts configuration.

Finally, we label the vector of all substructure parameters with $\theta_h \equiv \{m_{200,\text{sub}}, \vec{p}_{\text{sub}}, m_{200,\text{los}}, \vec{p}_{\text{los}}, z_{\text{los}}\}$, where we use bold letters to denote arrays (e.g. $m_{200,\text{sub}}$ is an ordered set of masses, one for each simulated subhalo) and bold letters with an arrow to indicate arrays of vectors (e.g. \vec{p}_{sub} is an ordered set of positions in the lens plane, one for each simulated subhalo).

2.4 Modelling free-streaming effects in WDM

The free-streaming effects of WDM are well described in terms of the half-mode wavelength λ_{hm} , which corresponds to the scale at which the DM transfer function falls to half the CDM transfer function. We can define the half-mode mass as the mass contained within a radius of the half-mode wavelength:

$$M_{\text{hm}} = \frac{4\pi\Omega_M\rho_{\text{crit}}}{3} \left(\frac{\lambda_{\text{hm}}}{2}\right)^3, \quad (11)$$

where Ω_M is the matter density parameter and ρ_{crit} is the critical density of the Universe. Following Schneider et al. (2012), the half-mode wavelength,

$$\lambda_{\text{hm}} = 2\pi a_{\text{hm}} \left(2^{\nu/5} - 1\right)^{-1/(2\nu)}, \quad (12)$$

is the scale below which the initial density perturbations are completely erased, with $\nu = 1.12$ and, assuming that all DM is warm,

$$a_{\text{hm}} = 0.049 \left(\frac{m_{\text{WDM}}}{\text{keV}}\right)^{-1.11} \left(\frac{\Omega_{\text{DM}}}{0.025}\right)^{0.11} \left(\frac{h}{0.7}\right)^{1.22} h^{-1} \text{Mpc}. \quad (13)$$

We then have a one-to-one mapping between the mass of the WDM particle and the half-mode mass. For strong lensing, the half-mode mass can be thought of as an effective cutoff mass below which the DM mass function is strongly suppressed. To model this suppression in the WDM mass function we adopt for both subhalos and LOS halos the functional form from Lovell (2020):

$$\frac{n_{\text{WDM}}}{n_{\text{CDM}}} = \left(1 + \left(\alpha \frac{M_{\text{hm}}}{m_{200}}\right)^{\beta}\right)^{\gamma}, \quad (14)$$

with best fit parameters $\alpha = 4.2$, $\beta = 2.5$, and $\gamma = 0.2$ for subhalos, $\alpha = 2.3$, $\beta = 0.8$, and $\gamma = 1$ for central halos.

2.4.1 Smoothing substructures

The observational signature of WDM is, thus, the absence of small-scale structures. However, in the current parameterization, this is accompanied by the removal of the corresponding mass enclosed in them, whereas in reality the mass will still be present but will be diffused throughout the smooth main halo. This effect is manifested in a correlation between the half-mode mass and the main-halo Einstein radius: suppressing more substructure leads to an increase in the inferred Einstein radius since the total mass of the system (within

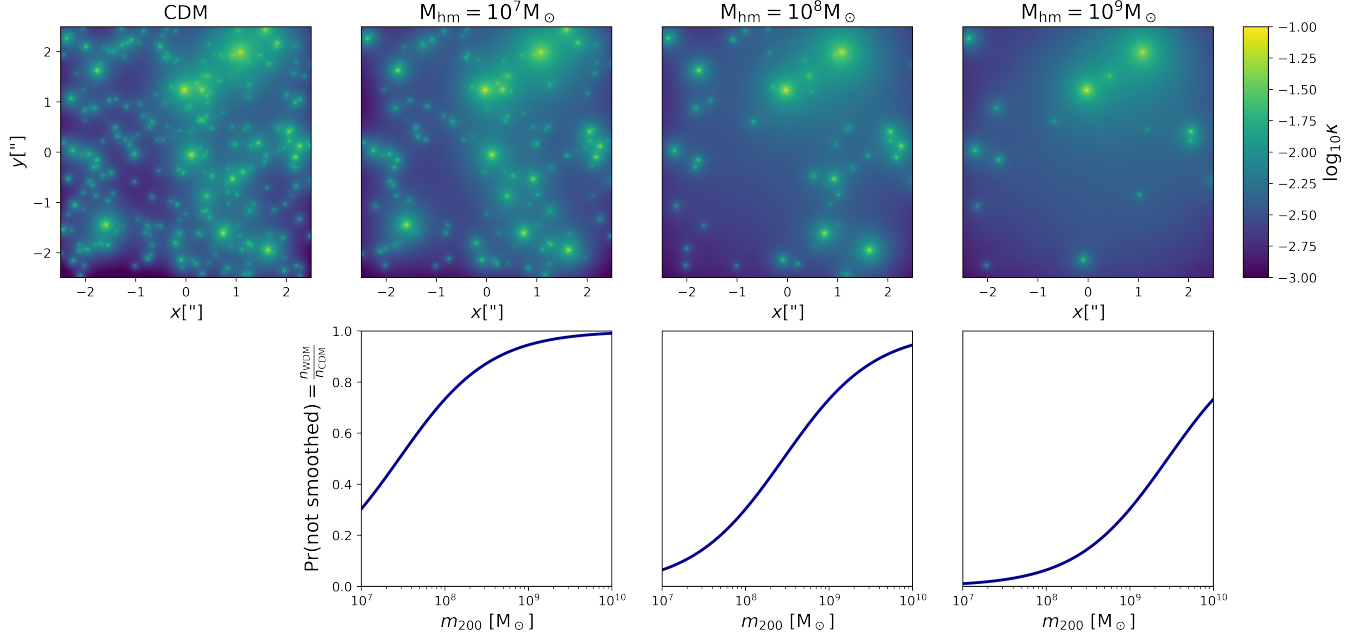


Figure 3. *Top:* Convergence maps for a population of LOS halos with masses sampled from the CDM HMF in the adopted mass range (Table 1) and projected in the lens plane following the prescription from Çagan Şengül et al. (2020). In the second to fourth columns we imitate the effect of WDM with different cutoff masses (as labelled in the titles) via our smoothing scheme. *Bottom:* We show the probability with which LOS halos do not get smoothed, equal to the ratio between the WDM and the CDM HMF (Equation 14). The smoothing is stochastic, so for each realization of the smoothing different halos are smoothed.

the image) is tightly constrained by the size of the observed ring (or arcs).

We introduce a prescription for dealing with this degeneracy, which well captures the physical reality of structure suppression due to free streaming. Halos that should be suppressed are not present because the DM particles that should make them up are freely streaming, and their mass is therefore more diluted throughout the main halo. Therefore, rather than removing or adding substructures as a response to a changing cutoff, we still sample substructures from the CDM mass function, but we smooth the displacement field generated by halos that should be suppressed based on the aforementioned prescription by Lovell (2020) to hide their lensing signature. In other words, each sampled small-scale halo has a probability equal to the ratio between the WDM and the CDM HMF (Equation 14) of not being smoothed.

We then effect the smoothing by convolving the deflection field of each individual sub-/LOS halo with a radially-symmetric filter

$$f \propto 1 - \exp\left(-\left(\frac{r}{r_{\text{smooth}}}\right)^{n_{\text{smooth}}}\right). \quad (15)$$

This filtering preserves the far-field lensing signature of the halo, which is only determined by its total mass. By default, we choose the smoothing scale to be equal to the halo virial radius: $r_{\text{smooth}} = r_{200}$, and the smoothing exponent $n_{\text{smooth}} = 2$.

In the top row of Figure 3 we visualize the convergence maps in the lens plane for the same realization of LOS halos drawn from CDM distributions (panel 1), and with different cutoff masses implemented with our smoothing scheme (panels 2-4). In the bottom row, we show how we decide to smooth the lensing signature of certain halos based on the ratio between the WDM and the CDM HMF (Equation 14).

3 STATISTICAL ANALYSIS

Constraining the fundamental properties of DM by characterizing the population of DM halos in a strong lensing image is an extremely difficult problem since the signal we are interested in has a sub-percent level influence on images dominated by statistical noise. The problem is further complicated by the large differences between images of different lensing systems.

Our ultimate goal is to compute the marginal posterior $p(\vartheta|\mathbf{x})$ for a single parameter of interest $\vartheta = M_{\text{hm}}$, the half mode mass, given an observation \mathbf{x} , for which we have the generative model

$$p(\mathbf{x}, \theta_s, \theta_l, \theta_h, \vartheta) = p(\mathbf{x}|\theta_s, \theta_l, \theta_h, \vartheta)p(\theta_s)p(\theta_l)p(\theta_h|\vartheta)p(\vartheta). \quad (16)$$

The first factor on the right-hand side is the simulator, while the other factors denote the priors on the various source, lens, and DM substructures parameters as listed in Table 1.

Therefore, in order to derive $p(\vartheta|\mathbf{x})$ we need to marginalise over all the nuisance parameters $\boldsymbol{\eta} \equiv \{\theta_l, \theta_s, \theta_h\}$:

$$p(\vartheta|\mathbf{x}) = \frac{p(\mathbf{x}|\vartheta)p(\vartheta)}{p(\mathbf{x})} = \frac{\int d\boldsymbol{\eta} p(\boldsymbol{\eta})p(\mathbf{x}|\vartheta, \boldsymbol{\eta})}{p(\mathbf{x})}p(\vartheta). \quad (17)$$

This is a very high-dimensional and multi-modal integral, even for simple analytical lens and source models, due to the large population of interchangeable substructures. Therefore, it is intractable, which renders likelihood-based inference infeasible in this case.

Instead, we approximate $p(\vartheta|\mathbf{x})$ using simulation-based inference with amortized approximate ratio estimators (Hermans et al. 2020). In particular, we employ the TMNRE algorithm developed by Miller et al. (2020, 2021) and implemented in the package *swyft*⁴.

⁴ <https://github.com/undark-lab/swyft>.

3.1 Marginal neural ratio estimation

MNRE (Miller et al. 2020) sets up a classification problem which produces an estimate of the likelihood-to-evidence ratio. This ratio estimator may then be used as a surrogate model to draw samples from an approximate posterior. The strategy is to train a classification network to discriminate between two hypotheses. In the first one, the observation \mathbf{x} and the parameter of interest θ are drawn jointly from the parameter prior and model: $\mathbf{x}, \theta \sim p(\mathbf{x}, \theta)$. In the second one, they are sampled marginally: $\mathbf{x}, \theta \sim p(\mathbf{x})p(\theta)$. Therefore, marginalization over nuisance variables η is done implicitly since the data will incorporate the variance from the nuisance parameters, but the inference procedure estimates only the marginal likelihood-to-evidence ratio. Training the classifier is done by minimizing the binary cross entropy via stochastic gradient descent. As a result, the trained network effectively learns the marginal likelihood-to-evidence ratios:

$$r(\mathbf{x}, \theta) \equiv \frac{p(\theta|\mathbf{x})}{p(\theta)} = \frac{p(\mathbf{x}|\theta)}{p(\mathbf{x})} = \frac{p(\mathbf{x}, \theta)}{p(\mathbf{x})p(\theta)}, \quad (18)$$

which we can use to evaluate the marginal posterior for the parameter of interest directly (if the prior PDF is known) or obtain samples otherwise.

3.2 Truncated marginal neural ratio estimation

Formally, inferring the marginal posterior for the substructure population parameter of interest would require marginalizing over all the source, lens and substructure realizations compatible with all possible strong lensing images. However, sampling lens and source parameters from their priors would require a very large amount of training data and a more complex network architecture when using neural ratio estimation. This has been attempted only in Brehmer et al. (2019) to infer the slope and normalization of the HMF. In order to reduce the complexity of the problem, since our main interest resides in sub-percent variations in the images, we propose to target one image (or a batch of images) at a time by first constraining its (theirs) lens and source parameters priors with TMNRE.

TMNRE generates a sequence of likelihood-to-evidence ratio estimators on both nuisance and parameters of interest for a specific observation \mathbf{x} . Between successive estimation steps, the prior is very conservatively truncated above a threshold to the region with the majority of the posterior mass. Subsequently, more training data is drawn. We set the threshold hyperparameter to $\epsilon = 10^{-5}$, which, in case of a Gaussian posterior, corresponds to truncating at $\sim 4.78 \sigma$ (Miller et al. 2021).

In particular, with TMNRE we target a restricted set of the nuisance parameters η : namely, those of the analytic smooth lens and source models, θ_l and θ_s , while leaving halo parameters, θ_h unconstrained.

To summarize, thanks to TMNRE, the overall analysis strategy splits into the following steps:

1. Train an inference network on an image \mathbf{x} to constrain the source and lens parameters, θ_s and θ_l , within ranges consistent with the observation. We then generate targeted training data based on this constrained model.
2. Train an inference network to learn the marginal likelihood-to-evidence ratio for our parameter of interest, the half mode mass M_{hm} , on the targeted training data.

Similarly to the reasoning behind the ABC rejection algorithm,

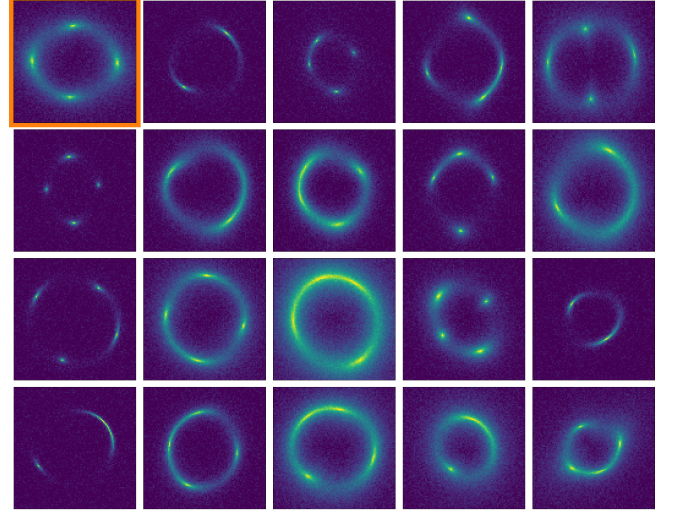


Figure 4. We present a gallery of twenty mock strong-lensing images we use as target observations. These mock observations have been generated with arbitrary lens and source parameters drawn from the initial prior in Table 1. Their peak SNR is ~ 30 , representative of HST data. We analyse these images by first constraining their lens and source parameters prior in subsection 4.3. Then, we combine them in order to infer the cutoff mass scale in subsection 4.4. For the first one (upper left corner, framed in orange) of these images we show our results of the first part of the pipeline (subsection 4.3) in Figure 6, Figure 7, and Figure 8.

which discards sampled parameters values if the generated data is too different from the observed data, we justify this approach by noting that parameters that do not produce observations similar to \mathbf{x} will not contribute to the integral in Equation 17. Restricting the input parameters in this way immensely reduces the variability of simulated data, which allows us to use simpler network architectures and fewer training examples in the next step. As a result, the inference is now *targeted* to the specific observation at hand rather than amortized over all the possible lens/source combinations from the full prior. We would like to point out that the inference is still locally amortized in the constrained prior region, and this enables empirical test of the inference result (see subsection 4.5).

4 RESULTS

In this section we show our results. First, we describe the simulated data in subsection 4.1 and the inference network architectures in subsection 4.2. We then show how we constrain the lens and source parameters in subsection 4.3. Next, we show our results for the cutoff mass and describe how we can combine the information from different strong lensing images in subsection 4.4. In the same subsection we show our results on the DM mass. Finally, we directly assess the statistical behaviour of the trained neural networks in subsection 4.5.

4.1 Mock data generation

We want our simulations to be representative of HST data, in order to demonstrate that our pipeline is in principle able to extract the signal of interest from them. We adopt a resolution of $0.05''$, being slightly larger than the expected $0.04''$, which allows us to disregard its point-spread function (PSF) (Gennaro 2018). The size of the images is 100×100 pixels, so they cover an area of $5 \times 5''$ on the sky.

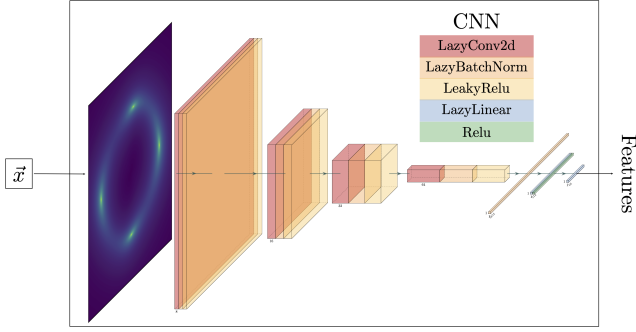


Figure 5. Illustration of the embedding CNN architecture used in the first part of the pipeline to constrain lens and source parameters. The observation \mathbf{x} gets compressed into features: estimates of the best possible data summary statistic, by the CNN. In describing the CNN layers we follow PyTorch (Paszke et al. 2019) convention. To create the illustration we have used Iqbal (2018).

Initially we generate the mock data with a resolution 10-times higher and then downsample it to the adopted resolution by local averaging, effectively simulating integration of the light across the pixel areas.

We model the instrumental effects by simply assuming a Gaussian and uncorrelated pixel noise. The noise level σ is set so that the peak SNR ratio of the image is ~ 30 (after downsampling), representative of HST data. Then, given a modelled flux, our simulator is given by:

$$p(\mathbf{x}|\theta_s, \theta_l, \theta_h, \vartheta) = \mathcal{N}(\mathbf{x}|\text{obs}(\theta_s, \theta_l, \theta_h, \vartheta), \sigma^2). \quad (19)$$

We leave to future works to account for the correct modeling of the PSF and correlated pixel noise.

In Figure 4 we show a gallery of twenty mock strong-lensing images we use as target observations. These mock observations have been generated with arbitrary lens and source parameters drawn from the initial prior in Table 1. Their peak SNR is ~ 30 , representative of HST data.

4.2 Inference network architecture

The inference neural network used to perform TMNRE is split into two different components: an embedding network $C_\phi(\mathbf{x})$ and a binary classification network. The embedding network compresses data into a low-dimensional feature vector, estimating the best possible summary statistics from the full input image. The binary classification network is the marginal classifier that performs the actual ratio estimation. It passes the featurized observational data concatenated with the parameter of interest into a multi-layers perceptron (MLP) to estimate the marginal likelihood-to-evidence ratios. The network architecture can be expressed as:

$$f_\phi(\mathbf{x}, \vartheta) = \text{MLP}_\phi(\text{features} = C_\phi(\mathbf{x}), \vartheta) = \ln r(\mathbf{x}, \vartheta). \quad (20)$$

For the embedding network, in both steps of the pipeline, we adopt a simple convolutional neural network (CNN). In Figure 5 we show the CNN architecture used to constrain lens and source parameters. The one used to estimate the cutoff mass has a similar structure.

4.3 Constraining lens and source parameters

We constrain lens and source parameters regions with TMNRE, as described in subsection 3.2, with multiple sampling and training rounds.

In total, we perform 6 sampling and training rounds. In each round, we simulate 10^5 observations, of which 90% are used as the training dataset, and the remaining 10% as the validation dataset. Evaluations of the network on the mock target image are used to truncate the prior after each round, so that the region for lens and source parameters is targeted. The first training round is performed on the dataset generated from the initial source and lens parameters priors, shown in Table 1. In Figure 6 we show the initial and constrained priors. It can be seen that after the first round just a few of the parameters priors get truncated, e.g. the Einstein radius. By having truncated these initial parameters, in the following rounds the other parameters can be better learned by the network and so constrained. In Figure 7, we show samples from the first five training datasets, which demonstrate that the constrained regions are indeed the ones that are likely to produce data similar to the targeted image \mathbf{x} . After the sixth round of training, it is not possible anymore to truncate the prior region based on the predetermined threshold, as seen in Figure 8. The truncation scheme has then efficiently identified the constrained region for lens and source parameters consistent with the targeted observation.

Using the last constrained dataset, it is then easier in the second step of the pipeline to train a marginal neural ratio estimator to perform the final inference on the cutoff mass, as explained in subsection 3.2.

We would like to stress that these constrained priors correctly account for lens and source parameters uncertainties. In all our simulated data, the substructure parameters θ_h are randomly sampled from their prior, in order to account for the presence of substructure. This has the desirable outcome of approximately accounting for the average effect that an additional mass component has on the main lens parameters (e.g. inferring an unbiased Einstein radius) and contributes to the source and lens uncertainties.

4.4 Dark matter inference

For the second step of the pipeline, we train an inference network to learn the cutoff mass on the last constrained dataset.

From initial tests, we have found that features from a single image are very hard to learn for the classifier, resulting in a very noisy ratio estimator. In order to reduce the estimator uncertainty, we then train the cutoff mass classifier on a dataset $X^N = \{\mathbf{x}_1, \dots, \mathbf{x}_N\}$ of N different observations. For each observation, first we constrain its lens and source parameters as explained in subsection 4.3. Then, we train the cutoff classifier on the concatenation of the features coming from their embedding networks, effectively learning $r(X^N, \vartheta)$. Note that the images in one dataset are sampled with the same cutoff mass M_{hm} , but different lens, source, and substructures realizations. In fact, our final goal is to apply the full pipeline to real data, which will all have different source, lens and substructures configurations, but will have encoded the same DM properties.

In the first row of Figure 9 we show the results from the inference network on ten test sets of lenses generated with a M_{hm} value of $10^7, 10^8, 10^9$ and $10^{10} M_\odot$. Each curve is the posterior obtained for a set of $N = 20$ lenses. Each of the mock observations has lens and source parameters sampled from their own final constrained prior, and different substructure population.

Now that we have reduced the estimator noise, it is straightforward to perform inference on a group of sets of images by combining their ratios. Given a dataset $X^N = \{\mathbf{x}_1, \dots, \mathbf{x}_N\}$ of images, the combined ratio for multiple M datasets is simply given by $r(X_M^N, \vartheta) \propto \prod_{i=1}^M r(X_i^N, \vartheta)$, where the proportionality is a ratio of evidences, independent of the parameter value, so it only accounts for a proper normalisation (Brehmer et al. 2019; Hermans et al. 2020). In the second row of Figure 9 we show the results for the

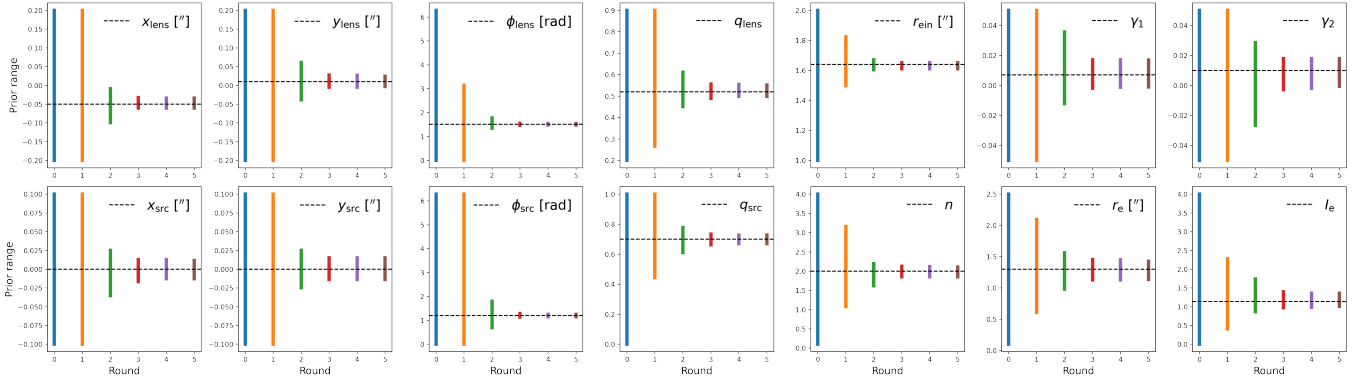


Figure 6. Constrained priors. Visualization of the sequential truncation of the lens and source priors over the 6 rounds of training. The particular target is the first mock image (framed in orange in Figure 4), whose parameters are depicted as black dashed horizontal lines.

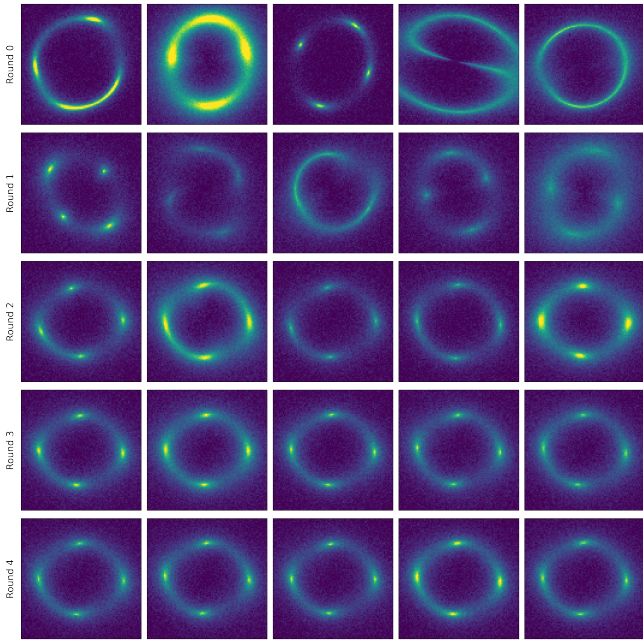


Figure 7. Training data targeting the first mock observation (framed in orange in Figure 4). In each row we show five examples of training data for the first five rounds. In the first round we sample our data from the initial prior shown in Table 1. For the following rounds, the data is sampled from the constrained priors, obtained by evaluating the network trained with the previous round dataset on our target observation (see subsection 4.3). It is evident that with each round the training data more closely resembles the target image \mathbf{x}

combination of the $M = 10$ different posteriors shown in the first column.

In the third row we show a combined posterior for the WDM mass function from 200 images ($M = 10$ sets of $N = 20$ images). These plots show the uncertainty in the subhalo mass function under the assumption that it has the functional form in Equation 14 with parameters from Lovell (2020).

These first results show that our method is sensitive to the low-mass end of the HMF, and that we have unbiased results from combining just 10 sets of 20 observations, given that in the second panel of Figure 9 the true input value for the half-mode mass M_{hm} is consistently contained within the estimated posterior. In subsection 4.5 we will

show a more sophisticated method to assess the statistical behaviour of our inference results.

In Figure 10 we show our results for the WDM mass. For each row we show the combined posterior of $M = 10$ sets of $N = 20$ observations in terms of the cutoff mass (as the second row in Figure 9), the WDM mass assuming a flat prior on the cutoff mass, and the WDM mass assuming a flat prior on the latter. Each row corresponds to a different cutoff mass value, and hence WDM mass value, given the mapping between these two quantities in subsection 2.4.

4.5 Credible interval testing

We would like to directly test and validate the statistical behaviour of our inference results by determining the expected coverage of the ratio estimator produced by the network. This can be easily done in *swyft* thanks to local amortization (Miller et al. 2021). The goal is to compare the nominal and empirical expected coverage probabilities of estimated Bayesian credible intervals, which should coincide for a well-calibrated estimator. For the statistical formalism and definition of credible region and expected coverage probability we refer the reader to Hermans et al. (2021). In brief, an ideal estimator has matching empirical and nominal expected coverage, a conservative one predicts lower credibility than empirically obtained, and an overconfident one has higher nominal than empirical credibility. In plots like Figure 11, the line for an ideal ratio estimator should perfectly align with the diagonal, whereas for a conservative (overconfident) estimator, it will lie above (below) the diagonal. In combination with visually checking the posteriors, this test supports the accuracy of the posterior estimator and is also particularly useful when one does not have access to the ground-truth against which to compare the results. In Figure 11 we show the empirical versus nominal expected coverage probabilities for the cutoff mass inference network. We can see that the inference network for the half-mode mass has converged with good expected coverage.

5 CONCLUSIONS

Strong gravitational lensing as a probe of the particle nature of DM has sparked much interest over the last few years. Moreover, the development of fast and accurate techniques to extract information from strong lensing images is well motivated by the wealth of new high-resolution strong lensing observations that will become available in the near-future.

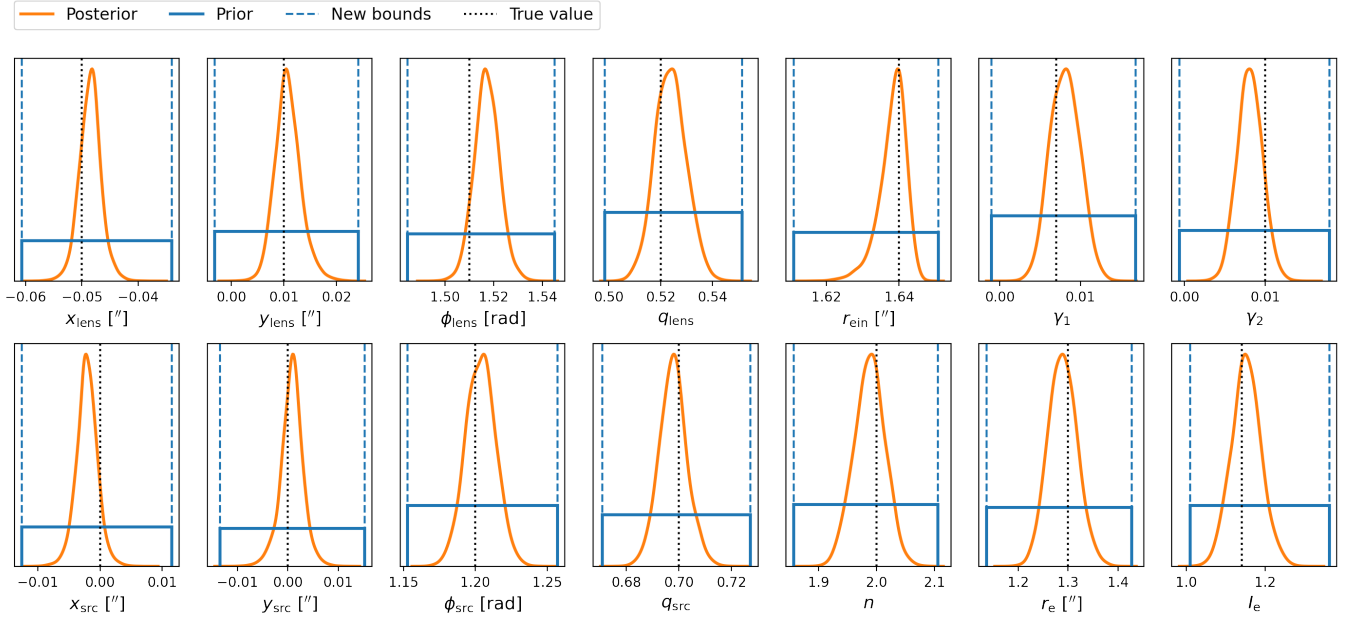


Figure 8. Lens and source parameters posteriors. In solid blue we show the last round constrained prior for the first (upper left corner, framed in orange) target image in Figure 4. The dotted black lines correspond to the true lens and source parameters values with which we have generated the target image. In orange we show the evaluated posteriors for lens and source parameters in the last training round. Based on the predetermined threshold, the new bounding limits (dashed blue) correspond to the full constrained prior region, so it is not possible anymore to constrain the prior.

In this work, we have presented the first step towards a new neural SBI pipeline (see section 3) to analyse present and future strong gravitational lensing systems in order to constrain the cutoff in the DM HMF, and so the DM mass. To this end, we have used a recent machine learning development, TMNRE, that makes it possible to *target* the analysis to a specific observation rather than amortize over all possible variations in lensing systems, making inference more efficient and precise. Thanks to TMNRE, we overcome the computational challenges of traditional MCMC, nested sampling and trans-dimensional MCMC methods, by directly learning the marginal posterior for the parameter of interest from the observation. TMNRE leverages neural networks to directly learn the best summary statistic possible from the full input data, without having to compress the observation into hand-crafted summary statistics. This work is then a step forward towards making the analysis of strong lensing images for DM science faster, more efficient and more accurate. In addition, our inference results can be validated with expected coverage tests (see subsection 4.5).

Our key results can be summarized as follows:

- Thanks to our targeted approach, we are able to correctly estimate the lens and source parameters uncertainties, accounting for the presence of substructures in the mass range $[10^7, 10^{10}] M_\odot$. We use the final lens and source parameters truncated prior (see subsection 4.3) to generate a targeted training dataset in order to infer the DM cutoff.
- In the case that DM is warm, we are able to infer the location of the cutoff in the HMF in the $[10^7, 10^{10}] M_\odot$ mass range by combining up to 200 observations (see subsection 4.4). We show our results in Figure 9. By construction, these results are correctly marginalized over model uncertainties and have proper expected coverage (see subsection 4.5).

- A cutoff mass posterior translates into a posterior on the WDM mass, given the mapping in subsection 2.4. We show our results in Figure 10 for a flat prior on the cutoff mass and a flat prior on the WDM mass. We obtain an expected 95% credible lower limits around 6.5 keV in the case of the scenario closest to CDM (see bottom left panel in Figure 10), given the adopted prior and the various assumptions of our simulation model that will be discussed below.

Throughout this study we have made a number of simplifying assumptions for the lens mass distribution, source light profile and substructure models. We have also neglected effects such as inadequate lens light subtraction, realistic PSF modelling and correlated pixel noise due to effects including the telescope's PSF. Before this analysis pipeline can be safely extended to real observations, these assumptions need to be correctly addressed. For example, a correct treatment would require adding potential corrections to the analytic lens mass model (Vegetti & Koopmans 2009a), adopting a more complex source model such as the non-parametric source light model introduced in (Coogan et al. 2020; Karchev et al. 2021), validating our smoothing scheme (subsubsection 2.4.1) to accurately account for DM free-streaming effects, and properly considering the PSF and correlated noise (Wagner-Carena et al. 2022). We believe there are no major obstacles in incorporating all of these components in our framework without fundamentally altering the inference procedure.

We would like to point out that the residuals between the image of an extended source lensed by the total lens potential (accounting for substructures), and that of the same source lensed only by the main lens component are proportional to the gradient of that source evaluated in the image plane (Cyr-Racine et al. 2019, Equation 16). We anticipate that using sources with more complex morphologies will result in higher sensitivity to the DM cutoff mass, given the ability to properly model these sources.

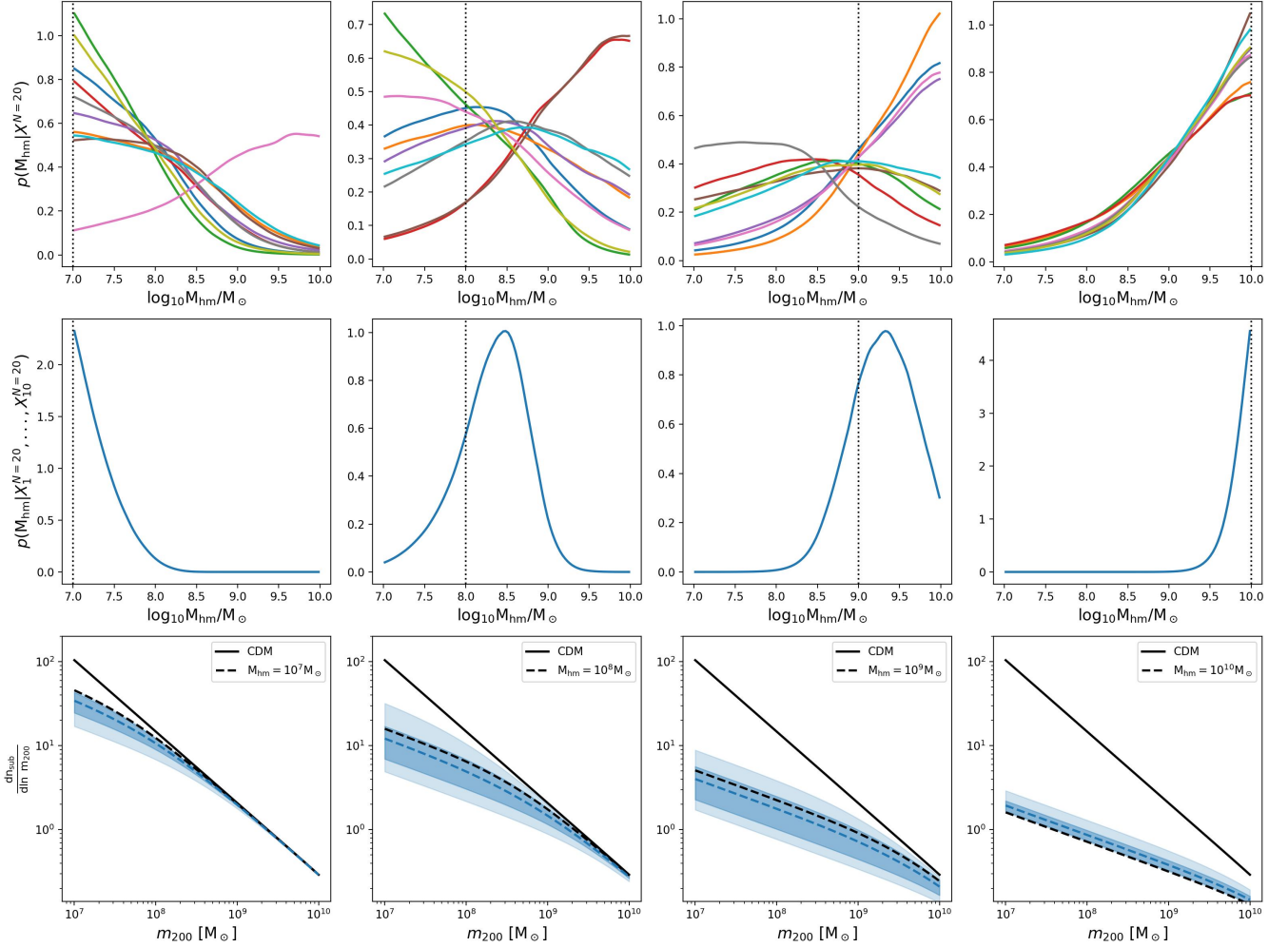


Figure 9. *Top:* Approximate posteriors for the half-mode mass derived from 10 different sets of 20 images. The dotted black line represents the true value of the half mode mass with which we have generated the images ($10^7, 10^8, 10^9, 10^{10} M_{\odot}$). *Middle:* We show the approximate posterior resulting from the combination of the $M = 10$ different posteriors shown in the first column, as explained in the text (subsection 4.4). *Bottom:* Subhalo mass function constraints derived from the cutoff mass posterior shown in the second column. The black solid line shows the CDM subhalo mass function according to Equation 9, whereas the black dashed line shows the WDM subhalo mass function according to Equation 14, given the true cutoff mass shown in the label. The blue shaded line shows the mean of the WDM subhalo mass function obtained by sampling 1000 samples from the cutoff mass posterior shown in the second panel and using this value in Equation 14. We also show the central 68 and 95 percentiles as shaded bands. These plots show how uncertain the subhalo mass function is under the assumption that it has the functional form in Equation 14 with parameters from Lovell (2020).

In this work we have demonstrated that, in principle, the DM cutoff mass signal can be statistically extracted from a population of small-scale dark matter halos by a neural network using TMNRE. In future works, we plan on studying the correlation between the cutoff mass and other HMF parameters, such as its normalization and slope, using, on one hand, more advanced modelling techniques (as specified above) on multi-band observations, and, on the other, better neural network architectures to target low SNR scenarios.

Finally, we note that, thanks to its flexibility, our pipeline can incorporate any arbitrary DM model, as long as it specifies the form of the HMF and the density profiles of individual substructures. We are optimistic that the presented Bayesian inference pipeline will be able to constrain the amount of substructures, pinning down DM nature, using both the strong lensing images that exist today and the wealth of new strong lensing data coming from near-future observatories.

ACKNOWLEDGEMENTS

We thank Benjamin Kurt Miller and Elias Dubbeldam for helpful discussions.

This work is part of a project that has received funding from the European Research Council (ERC) under the European Union’s Horizon 2020 research and innovation program (Grant agreement No. 864035).

A.C. received funding from the Netherlands eScience Center (grant number ETEC.2019.018) and the Schmidt Futures Foundation. C.C. acknowledges the support of the Dutch Research Council (NWO Veni 192.020).

This work was carried out on the Lisa Compute Cluster at SURF-sara. We acknowledge the use of the python (Van Rossum & Drake Jr 1995) modules, matplotlib (Hunter 2007), seaborn (Waskom 2021), numpy (Harris et al. 2020), scipy (Virtanen et al. 2020), AstroPy (Astropy Collaboration et al. 2018), PyTorch (Paszke et al.

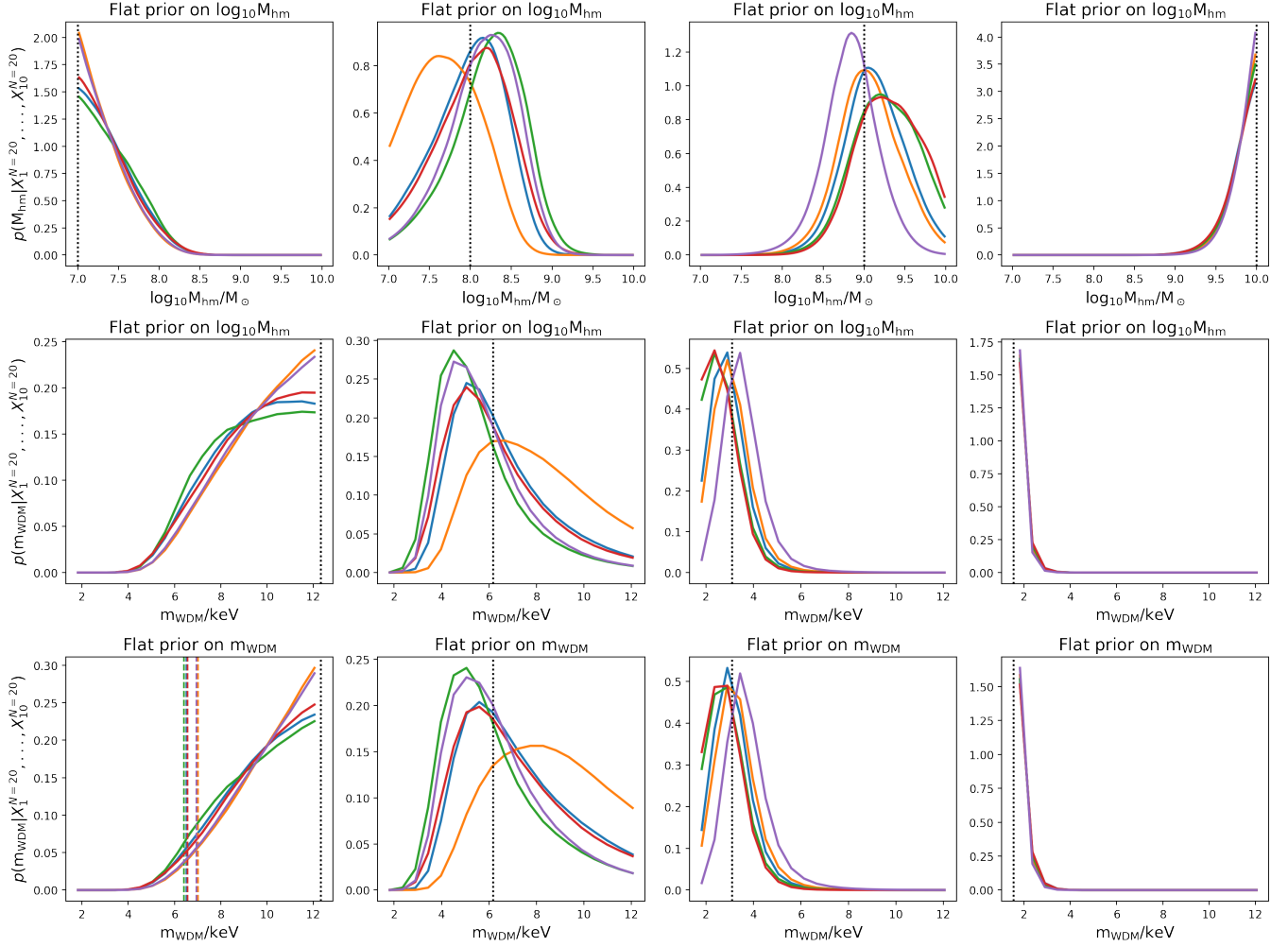


Figure 10. *Top:* We show five examples of combined posterior of $M = 10$ sets of $N = 20$ observations in terms of the cutoff mass (as the second row in Figure 9). The dotted black line represents the true value of the half mode mass with which we have generated the mock observations ($10^7, 10^8, 10^9, 10^{10} M_\odot$). *Middle:* Same results as shown in the first column but for the WDM mass, given the mapping between DM cutoff and DM mass in subsection 2.4, assuming a flat prior on the cutoff mass. *Bottom:* Same results as shown in the first column but for the WDM mass and assuming a flat prior on the latter. In the first plot of the row we show for the five examples the expected 95% credible lower limit on the WDM mass for the highest value of our prior distribution.

2019), Pyro (Bingham et al. 2019), `tqdm` (da Costa-Luis et al. 2021), and `jupyter` (Kluyver et al. 2016).

DATA AVAILABILITY

The data underlying this article will be shared on reasonable request to the corresponding author.

REFERENCES

- Abolfathi B., et al., 2021, *The Astrophysical Journal Supplement Series*, 253, 31
- Ade P. A. R., et al., 2016, *Astronomy & Astrophysics*, 594, A13
- Alexander S., Gleyzer S., McDonough E., Toomey M. W., Usai E., 2020, *The Astrophysical Journal*, 893, 15
- Amorisco N. C., et al., 2021, *Monthly Notices of the Royal Astronomical Society*, 510, 2464
- Astropy Collaboration et al., 2018, *AJ*, 156, 123
- Baltz E. A., Marshall P., Oguri M., 2009, *Journal of Cosmology and Astroparticle Physics*, 2009, 015–015
- Barnabe M., Koopmans L. V. E., 2007, *The Astrophysical Journal*, 666, 726–746
- Bayer D., Chatterjee S., Koopmans L. V. E., Vegetti S., McKean J. P., Treu T., Fassnacht C. D., 2018, Observational constraints on the sub-galactic matter-power spectrum from galaxy-galaxy strong gravitational lensing ([arXiv:1803.05952](https://arxiv.org/abs/1803.05952))
- Bingham E., et al., 2019, *J. Mach. Learn. Res.*, 20, 28:1
- Birrer S., Amara A., Refregier A., 2017, *Journal of Cosmology and Astroparticle Physics*, 2017, 037–037
- Bolton A. S., Burles S., Koopmans L. V. E., Treu T., Moustakas L. A., 2006, *The Astrophysical Journal*, 638, 703–724
- Bond J. R., Szalay A. S., Turner M. S., 1982, *Phys. Rev. Lett.*, 48, 1636
- Boyersky A., Drewes M., Lasserre T., Mertens S., Ruchayskiy O., 2019, *Progress in Particle and Nuclear Physics*, 104, 1–45
- Brehmer J., Mishra-Sharma S., Hermans J., Louppe G., Cranmer K., 2019, *The Astrophysical Journal*, 886, 49
- Brennan S., Benson A. J., Cyr-Racine F.-Y., Keeton C. R., Moustakas L. A., Pullen A. R., 2019, *Monthly Notices of the Royal Astronomical Society*, 488, 5085–5092

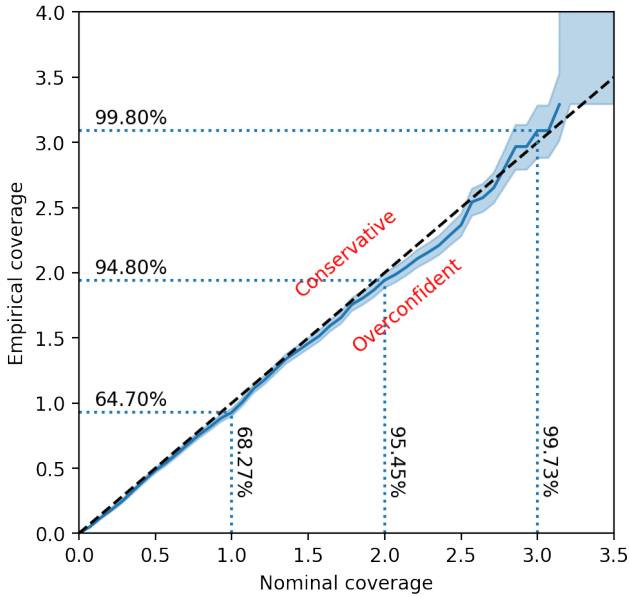


Figure 11. Empirical versus nominal expected coverage probabilities for the cutoff mass inference network. In case the line lies above (below) the black dashed diagonal line, the credible intervals are conservative (overconfident) and contain the true value with a frequency higher (lower) than nominally expected. We show the empirical (nominal) probabilities as horizontal (vertical) text.

Brewer B. J., Huijser D., Lewis G. F., 2015, Trans-Dimensional Bayesian Inference for Gravitational Lens Substructures ([arXiv:1508.00662](#))

Brownstein J. R., et al., 2011, *The Astrophysical Journal*, 744, 41

Bullock J. S., 2010, Notes on the Missing Satellites Problem, [doi:10.48550/ARXIV.1009.4505](#), <https://arxiv.org/abs/1009.4505>

Chatterjee S., Koopmans L. V. E., 2017, *Monthly Notices of the Royal Astronomical Society*, 474, 1762–1772

Ciotti L., Bertin G., 1999, Analytical properties of the $R^{1/m}$ luminosity law ([arXiv:astro-ph/9911078](#))

Cole A., Miller B. K., Witte S. J., Cai M. X., Grootes M. W., Nattino F., Weniger C., 2021, Fast and Credible Likelihood-Free Cosmology with Truncated Marginal Neural Ratio Estimation ([arXiv:2111.08030](#))

Colin P., Avila-Reese V., Valenzuela O., 2000, *The Astrophysical Journal*, 542, 622–630

Coogan A., Karchev K., Weniger C., 2020, Targeted Likelihood-Free Inference of Dark Matter Substructure in Strongly-Lensed Galaxies ([arXiv:2010.07032](#))

Coogan A., Correa C., Karchev K., Anau Montel N., Weniger C., 2022, Characterizing subhalos in strong gravitational lenses with truncated marginal neural ratio estimation

Cranmer K., Brehmer J., Louppe G., 2020, The frontier of simulation-based inference ([arXiv:1911.01429](#))

Cyr-Racine F.-Y., Keeton C. R., Moustakas L. A., 2019, *Physical Review D*, 100

Dalal N., Kochanek C. S., 2002, *The Astrophysical Journal*, 572, 25–33

Daylan T., Cyr-Racine F.-Y., Rivero A. D., Dvorkin C., Finkbeiner D. P., 2018, *The Astrophysical Journal*, 854, 141

Despali G., Vegetti S., 2017, *Monthly Notices of the Royal Astronomical Society*, 469, 1997–2010

Despali G., Vegetti S., White S. D. M., Giocoli C., van den Bosch F. C., 2018, *Monthly Notices of the Royal Astronomical Society*, 475, 5424–5442

Díaz Rivero A., Dvorkin C., 2020, *Physical Review D*, 101

Díaz Rivero A., Cyr-Racine F.-Y., Dvorkin C., 2018, *Physical Review D*, 97

Drlica-Wagner A., et al., 2019, Probing the Fundamental Nature of Dark

Matter with the Large Synoptic Survey Telescope ([arXiv:1902.01055](#))

Díaz Rivero A., Dvorkin C., Cyr-Racine F.-Y., Zavala J., Vogelsberger M., 2018, *Physical Review D*, 98

Enzi W., Vegetti S., Despali G., Hsueh J.-W., Benton Metcalf R., 2020, *Monthly Notices of the Royal Astronomical Society*, 496, 1718–1729

Gardner J. P., et al., 2006, *Space Science Reviews*, 123, 485–606

Gennaro M., 2018, in , Vol. 4, WFC3 Data Handbook v. 4. p. 4

Gilman D., Birrer S., Treu T., Keeton C. R., Nierenberg A., 2018, *Monthly Notices of the Royal Astronomical Society*, 481, 819–834

Gilman D., Birrer S., Treu T., Nierenberg A., Benson A., 2019a, *Monthly Notices of the Royal Astronomical Society*, 487, 5721–5738

Gilman D., Birrer S., Nierenberg A., Treu T., Du X., Benson A., 2019b, *Monthly Notices of the Royal Astronomical Society*, 491, 6077–6101

Giocoli C., Tormen G., Sheth R. K., van den Bosch F. C., 2010, *Monthly Notices of the Royal Astronomical Society*

Grazian C., Fan Y., 2019, A review of Approximate Bayesian Computation methods via density estimation: inference for simulator-models ([arXiv:1909.02736](#))

Harris C. R., et al., 2020, *Nature*, 585, 357–362

He Q., et al., 2020, A forward-modelling method to infer the dark matter particle mass from strong gravitational lenses ([arXiv:2010.13221](#))

He Q., et al., 2021, Galaxy-galaxy strong lens perturbations: line-of-sight haloes versus lens subhaloes ([arXiv:2110.04512](#))

Hermans J., Begy V., Louppe G., 2020, Likelihood-free MCMC with Amortized Approximate Ratio Estimators ([arXiv:1903.04057](#))

Hermans J., Delaunoy A., Rozet F., Wehenkel A., Louppe G., 2021, Averting A Crisis In Simulation-Based Inference ([arXiv:2110.06581](#))

Hezaveh Y. D., et al., 2016a, *The Astrophysical Journal*, 823, 37

Hezaveh Y., Dalal N., Holder G., Kisner T., Kuhlen M., Levasseur L. P., 2016b, *Journal of Cosmology and Astroparticle Physics*, 2016, 048–048

Hezaveh Y. D., Levasseur L. P., Marshall P. J., 2017, *Nature*, 548, 555–557

Hsueh J.-W., Fassnacht C. D., Vegetti S., McKean J. P., Spingola C., Auger M. W., Koopmans L. V. E., Lagattuta D. J., 2016, *Monthly Notices of the Royal Astronomical Society: Letters*, 463, L51–L55

Hsueh J.-W., et al., 2017, *Monthly Notices of the Royal Astronomical Society*, 469, 3713–3721

Hsueh J.-W., Enzi W., Vegetti S., Auger M. W., Fassnacht C. D., Despali G., Koopmans L. V. E., McKean J. P., 2019, *Monthly Notices of the Royal Astronomical Society*, 492, 3047–3059

Hunter J. D., 2007, *Computing in Science Engineering*, 9, 90

Iqbal H., 2018, HarisIqbal88/PlotNeuralNet v1.0.0, [doi:10.5281/zenodo.2526396](#), <https://doi.org/10.5281/zenodo.2526396>

Karchev K., Coogan A., Weniger C., 2021, Strong-lensing source reconstruction with variationally optimised Gaussian processes ([arXiv:2105.09465](#))

Kluyver T., et al., 2016, in Loizides F., Schmidt B., eds, Positioning and Power in Academic Publishing: Players, Agents and Agendas. pp 87–90

Klypin A., Kravtsov A. V., Valenzuela O., Prada F., 1999, *The Astrophysical Journal*, 522, 82–92

Kochanek C. S., 2004, The Saas Fee Lectures on Strong Gravitational Lensing ([arXiv:astro-ph/0407232](#))

Koopmans L., 2005, *EAS Publications Series*, 20, 161–166

Koopmans L., Browne I., Jackson N., 2004, *New Astronomy Reviews*, 48, 1085–1094

Laureijs R., et al., 2011, Euclid Definition Study Report ([arXiv:1110.3193](#))

Lovell M. R., 2020, *The Astrophysical Journal*, 897, 147

Lovell M. R., Frenk C. S., Eke V. R., Jenkins A., Gao L., Theuns T., 2014, *Monthly Notices of the Royal Astronomical Society*, 439, 300–317

Mao S., Schneider P., 1998, *Monthly Notices of the Royal Astronomical Society*, 295, 587–594

McKean J. P., et al., 2015, Strong gravitational lensing with the SKA ([arXiv:1502.03362](#))

Meneghetti M., 2016, Introduction to Gravitational Lensing

Miller B. K., Cole A., Louppe G., Weniger C., 2020, Simulation-efficient marginal posterior estimation with swyft: stop wasting your precious time ([arXiv:2011.13951](#))

Miller B. K., Cole A., Forrè P., Louppe G., Weniger C., 2021, Truncated

Marginal Neural Ratio Estimation ([arXiv:2107.01214](https://arxiv.org/abs/2107.01214))

Moore B., Ghigna S., Governato F., Lake G., Quinn T., Stadel J., Tozzi P., 1999, *The Astrophysical Journal*, 524, L19

Morningstar W. R., et al., 2019, *The Astrophysical Journal*, 883, 14

Navarro J. F., Frenk C. S., White S. D. M., 1997, *The Astrophysical Journal*, 490, 493–508

Nierenberg A. M., Treu T., Wright S. A., Fassnacht C. D., Auger M. W., 2014, *Monthly Notices of the Royal Astronomical Society*, 442, 2434–2445

Nierenberg A. M., et al., 2017, *Monthly Notices of the Royal Astronomical Society*, 471, 2224–2236

Paszke A., et al., 2019, in Wallach H., Larochelle H., Beygelzimer A., d'Alché-Buc F., Fox E., Garnett R., eds., *Advances in Neural Information Processing Systems 32*. Curran Associates, Inc., pp 8024–8035, <http://papers.neurips.cc/paper/9015-pytorch-an-imperative-style-high-performance-deep-learning-library.pdf>

Peebles P. J. E., 1982, *ApJ*, 263, L1

Perreault Levasseur L., Hezaveh Y. D., Wechsler R. H., 2017, *The Astrophysical Journal*, 850, L7

Refregier A., Amara A., Kitching T. D., Rassat A., Scaramella R., Weller J., 2010, *Euclid Imaging Consortium Science Book* ([arXiv:1001.0061](https://arxiv.org/abs/1001.0061))

Richings J., Frenk C., Jenkins A., Robertson A., Schaller M., 2021, *Monthly Notices of the Royal Astronomical Society*, 501, 4657–4668

Ritondale E., Vegetti S., Despali G., Auger M. W., Koopmans L. V. E., McKean J. P., 2019, *Monthly Notices of the Royal Astronomical Society*, 485, 2179–2193

Rubin V. C., Ford W. K. J., Thonnard N., 1980, *ApJ*, 238, 471

Schneider P., Sluse D., 2014, *Astronomy & Astrophysics*, 564, A103

Schneider A., Smith R. E., Macciò A. V., Moore B., 2012, *Monthly Notices of the Royal Astronomical Society*, 424, 684–698

Sérsic J. L., 1963, *Boletín de la Asociación Argentina de Astronomía La Plata Argentina*, 6, 41

Simon J. D., et al., 2019, *Testing the Nature of Dark Matter with Extremely Large Telescopes* ([arXiv:1903.04742](https://arxiv.org/abs/1903.04742))

Springel V., et al., 2008, *Monthly Notices of the Royal Astronomical Society*, 391, 1685–1711

Suyu S. H., Marshall P. J., Blandford R. D., Fassnacht C. D., Koopmans L. V. E., McKean J. P., Treu T., 2009, *The Astrophysical Journal*, 691, 277–298

Taylor A. N., Dye S., Broadhurst T. J., Benítez N., van Kampen E., 1998, *The Astrophysical Journal*, 501, 539–553

Tinker J., Kravtsov A. V., Klypin A., Abazajian K., Warren M., Yepes G., Gottlöber S., Holz D. E., 2008, *The Astrophysical Journal*, 688, 709–728

Unruh S., Schneider P., Sluse D., 2017, *Astronomy & Astrophysics*, 601, A77

Van Rossum G., Drake Jr F. L., 1995, *Python reference manual*. Centrum voor Wiskunde en Informatica Amsterdam

Vegetti S., Koopmans L. V. E., 2009a, *Monthly Notices of the Royal Astronomical Society*, 392, 945–963

Vegetti S., Koopmans L. V. E., 2009b, *Monthly Notices of the Royal Astronomical Society*, 400, 1583–1592

Vegetti S., Czoske O., Koopmans L. V. E., 2010a, *Monthly Notices of the Royal Astronomical Society*, 407, 225–231

Vegetti S., Koopmans L. V. E., Bolton A., Treu T., Gavazzi R., 2010b, *Monthly Notices of the Royal Astronomical Society*, 408, 1969–1981

Vegetti S., Lagattuta D. J., McKean J. P., Auger M. W., Fassnacht C. D., Koopmans L. V. E., 2012, *Nature*, 481, 341–343

Vegetti S., Koopmans L. V. E., Auger M. W., Treu T., Bolton A. S., 2014, *Monthly Notices of the Royal Astronomical Society*, 442, 2017–2035

Vegetti S., Despali G., Lovell M. R., Enzi W., 2018, *Monthly Notices of the Royal Astronomical Society*, 481, 3661–3669

Virtanen P., et al., 2020, *Nature Methods*, 17, 261–272

Wagner-Carena S., Aalbers J., Birrer S., Nadler E. O., Darragh-Ford E., Marshall P. J., Wechsler R. H., 2022, *From Images to Dark Matter: End-To-End Inference of Substructure From Hundreds of Strong Gravitational Lenses* ([arXiv:2203.00690](https://arxiv.org/abs/2203.00690))

Waskom M. L., 2021, *Journal of Open Source Software*, 6, 3021

Zwicky F., 1933, *Helv. Phys. Acta*, 6, 110

Çağan Şengül A., Tsang A., Diaz Rivero A., Dvorkin C., Zhu H.-M., Seljak U., 2020, *Physical Review D*, 102

da Costa-Luis C., et al., 2021, tqdm: A fast, Extensible Progress Bar for Python and CLI, [doi:10.5281/zenodo.5517697](https://doi.org/10.5281/zenodo.5517697), <https://doi.org/10.5281/zenodo.5517697>

APPENDIX A: SÉRSIC SOURCE

Here we describe the elliptical coordinates (r_x, r_y) , the normalization k_n and the index n that enter in the modeling of the Sérsic profile in Equation 6.

The transformation from Cartesian (x, y) to elliptical coordinates (r_x, r_y) is given by

$$\begin{pmatrix} r_x \\ r_y \end{pmatrix} = \begin{pmatrix} \sqrt{q} & 0 \\ 0 & 1/\sqrt{q} \end{pmatrix} \begin{pmatrix} \cos \phi_s & \sin \phi_s \\ -\sin \phi_s & \cos \phi_s \end{pmatrix} \begin{pmatrix} x - x_0 \\ y - y_0 \end{pmatrix}, \quad (\text{A1})$$

where ϕ_s is the rotation angle, q_s is the axis ratio, and (x_0, y_0) is the center of light position.

The normalization k_n is related to the index n by an implicit transcendental equation in terms of the complete and lower incomplete gamma functions $2\gamma(2n, k_n) = \Gamma(2n)$. We use the expansion in series from Ciotti & Bertin (1999), valid over a wide range of indices n , stopping at order $\mathcal{O}(n^{-3})$.

APPENDIX B: LINE-OF-SIGHT HALOS AS EFFECTIVE SUBHALOS

Following Çağan Şengül et al. (2020), LOS halos at comoving distance χ can be treated as subhalos on the main-lens plane with an effective projected mass density given by:

$$\Sigma_{\chi, \text{eff}}(D_I \vec{x}; m_{200}, r_s, \tau) = \Sigma(D_I \vec{x}; m_{200, \text{eff}}, r_{s, \text{eff}}, \tau). \quad (\text{B1})$$

The effective scale radius $r_{s, \text{eff}}$ and mass $m_{200, \text{eff}}$ are respectively

$$r_{s, \text{eff}} = \frac{D_I}{g(\chi) D_\chi} r_s, \quad (\text{B2})$$

and

$$m_{200, \text{eff}} = f(\chi) \frac{\Sigma_{\text{cr}, l}}{\Sigma_{\text{cr}, \chi}} \left(\frac{D_I}{g(\chi) D_\chi} \right)^2 m_{200}. \quad (\text{B3})$$

The piecewise functions $f(\chi)$ and $g(\chi)$ are:

$$f(\chi) = \begin{cases} 1 - \beta_{\chi l} & \chi \leq \chi_l \\ 1 - \beta_{l\chi} & \chi > \chi_l \end{cases}, \quad (\text{B4})$$

and

$$g(\chi) = \begin{cases} 1 & \chi \leq \chi_l \\ 1 - \beta_{l\chi} & \chi > \chi_l \end{cases}, \quad (\text{B5})$$

with $\beta_{ij} = \frac{D_{ij} D_s}{D_j D_{is}}$, where D_i is the angular diameter distance from the observer to plane i , and D_{ij} is the angular diameter distance from lens plane i to lens plane j , and χ_l is the comoving distance to the main-lens plane. We have also introduced the critical surface density at plane i

$$\Sigma_{\text{cr}, i} \equiv \frac{c^2 D_s}{4\pi G D_i D_{is}}. \quad (\text{B6})$$

This paper has been typeset from a \LaTeX file prepared by the author.